Electronic Structure of Metalloporphenes, Antiaromatic Analogs of Graphene

Ivan Pavlak,[a] Lujo Matasović,[b] Eric A. Buchanan,[c] Josef Michl,[c,d] and Igor Rončević*[d,e]

[a] Department of Chemistry, Faculty of Science, University of Zagreb, Horvatovac 102A, 10000 Zagreb, Croatia
[b] Cavendish Laboratory, Department of Physics, University of Cambridge, J. J. Thomson Avenue, Cambridge, CB3 0HE, UK
[c] Department of Chemistry and Biochemistry, University of Colorado, 80309-0215 Boulder, CO, United States
[d] Institute of Organic Chemistry and Biochemistry of the CAS, Flemingovo nám. 2, 16610 Prague 6, Czech Republic
[e] Department of Chemistry, University of Oxford, Chemistry Research Laboratory, Oxford OX1 3TA, UK

KEYWORDS: antiaromaticity, two-dimensional materials, porphyrin nanostructures, Peierls distortion, covalent organic frameworks, exact exchange

ABSTRACT: Zinc porphene is a two-dimensional material made of fully fused zinc porphyrins in a tetragonal lattice. It has a fully conjugated π system, making it similar to graphene. Zinc porphene has recently been synthesized and shown to be a semiconductor (*Nat. Comm.*, **2023**, *14*, 6308.). This is in contrast with all previous predictions of its electronic structure, which indicated metallic conductivity. We show that the gap-opening in zinc porphene is caused by a Peierls distortion of its unit cell from square to rectangular, thus giving the first account of its electronic structure in agreement with experiment. Accounting for this distortion requires a proper treatment of electron delocalization, which can be done using hybrid functionals with a substantial amount of exact exchange. Such a functional, PBE38, is then applied to predict the properties of many first transition row metalloporphenes, some of which have already been prepared. We find that changing the metal strongly affects the electronic structure of metalloporphenes, resulting in a rich variety of both metallic conductors and semiconductors, which may be of great of interest to molecular electronics and spintronics. Properties of these materials are mostly governed by the extent of the Peierls distortion and the number of electrons in their π system, analogous to changes in aromaticity observed in cyclic conjugated molecules upon oxidation or reduction. These results give an account of how the concept of antiaromaticity can be extended to periodic systems.

INTRODUCTION

Two-dimensional (2D) polymers have been extensively investigated due to their promising applications as optoelectronic materials, molecular magnets, energy storage media, electrocatalysts, etc.[1-8] The archetypal 2D material is graphene, which displays remarkable mechanical and electronic properties due to a fully conjugated π system.[9, 10] However, stoichiometric functionalization of graphene remains a towering obstacle in the path towards tunable π-conjugated 2D materials.[11, 12]

Recently, we have succeeded in the synthesis of porphene, a graphene analog made of fully fused porphyrin rings (Figure 1).[13] Both graphene and porphene are fully conjugated, but they have two key differences. One, graphene has a hexagonal lattice while porphene is composed of roughly square porphyrin monomers. A half-filled square lattice is known to be susceptible to distortion,[14] suggesting that the shape of the porphene unit cell may depend on the number of electrons in its π system. To draw a parallel to molecules, graphene can be thought as a periodic analog of the aromatic high-symmetry benzene,[15,16, 17] while porphene resembles antiaromatic cyclobutadiene, which adopts a lower-symmetry rectangular geometry. This was first noted by Osuka and collaborators on a 2×2 fragment of zinc porphene (Figure 1b).[18]

The second, more practically important difference between graphene and porphene is that the latter offers a straightforward avenue for tuning. Different metalloporphenes (**MP**) can be produced from free-base porphene by controlled reversible insertion of a metal ion, **M**, into the center of each macrocycle, without taking any π centers out of conjugation.[14] Given the wide choice of metals M in different spin states and possible axial ligands **X**, porphene offers unprecedented opportunity for stoichiometric functionalization. Availability of bidentate ligands suggests that controlled stacking into periodic multilayers

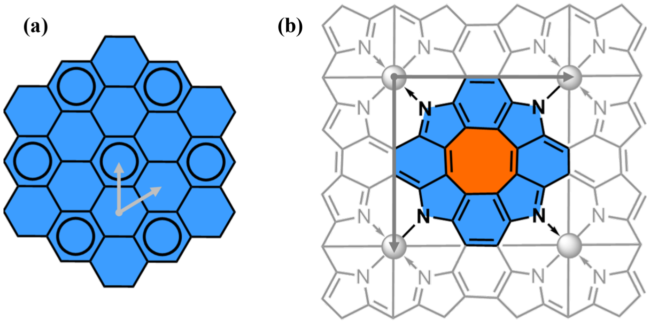

Figure 1. Structure of (a) graphene and (b) a metalloporphene (MP), with lattice vectors shown with grey arrows. Aromatic and antiaromatic rings are shown in blue and orange, respectively.

may be within reach. Since metal ions can be introduced into porphene and removed under controlled conditions, nanolithographic writing of patterns and design of circuitry for applications in electronics, spintronics, photonics, and elsewhere can be imagined. The ultimate resolution of this canvas for molecular painting is 8.4 Å, the closest distance between two metal centers in a metalloporphene.

To take full advantage of the opportunities offered by this synthetic advance, it is important to obtain guidance from theory concerning metalloporphene properties as a function of choice of metal and ligands. Such calculations have been published before,[19-24] but they invariably predicted zinc porphene (**ZnP**) to be a square metallic conductor. This is in disagreement with our experimental results on **ZnP**, which indicated an absence of metallic conductivity and showed a presence of infrared-active vibrations, revealing that **ZnP** is in fact a semiconductor (nonzero band gap).[14] In section **A** of this paper, we show that an appropriate level of theory can account for the observed semiconducting nature of **ZnP**, and in section **B** we systematically investigate the electronic structure and geometry of metalloporphenes containing elements from the first transition row of the periodic table, Sc–Zn, revealing a rich landscape of tunable materials.

RESULTS AND DISCUSSION

A. Symmetry breaking in ZnP. Metalloporphenes such as ZnP are composed of both aromatic circuits (pyrrole and benzene, shown in blue in Figure 1) with delocalized π bonds, and antiaromatic circuits (cylooctatetraene, orange) with distinctly localized bonds.[18] This leads to mixed aromaticity (or concealed antiaromaticity[25]), suggesting that both types of circuits need to be described with a similar level of accuracy to properly capture their electronic structure. All previous investigations of ZnP[19-22] used pure density functional theory (DFT) to optimize its geometry, predicting a D_{4h} (square) unit cell with a single minimum. Subsequent band structure calculations on this square minimum always yielded a gapless band structure, in contrast with experiment[14] as well as with the observation that 2D materials with square lattices are exceedingly rare.[26, 27]

This discrepancy between theory and experiment may be explained by recognizing that pure DFT overemphasizes delocalisation.[27] In terms of the semiempirical Hubbard model,[28] pure DFT underestimates U (the energy lost when two electrons occupy the same site) and overestimates the hopping integral t (the energy gained when an electron is free to move between sites). This leads to a too small U/t ratio, overemphasizing delocalization.[29]

Hybrid DFT can provide a better balance between localization (U) and delocalization (t) by including some percentage (usually 20–50%) of exact exchange (EE), which lowers the energy of all same-spin electron pairs. Therefore, the addition of EE promotes localization, or increases U/t, which comes at the expense of increased computation time and worse description of static correlation.[30]

By admixing different proportions of EE to the pure PBE (Perdew-Burke-Ernzerhof[31]) functional, we found that at least 35% EE is necessary to break the square symmetry and open a band gap in **ZnP** (Figure 2). Similar results were obtained in case of cyclo[18]carbon (an 18-membered all-carbon ring) and butadiyne-linked Zn porphyrin nanorings, which both require 30-35% EE to optimize to the experimentally found symmetry-broken geometries.[32, 33] For these reasons, all subsequent work presented here was done using the PBE38 (37.5% exact exchange) functional, which was also found to be the optimal proportion of EE in several benchmarks.[34, 35]

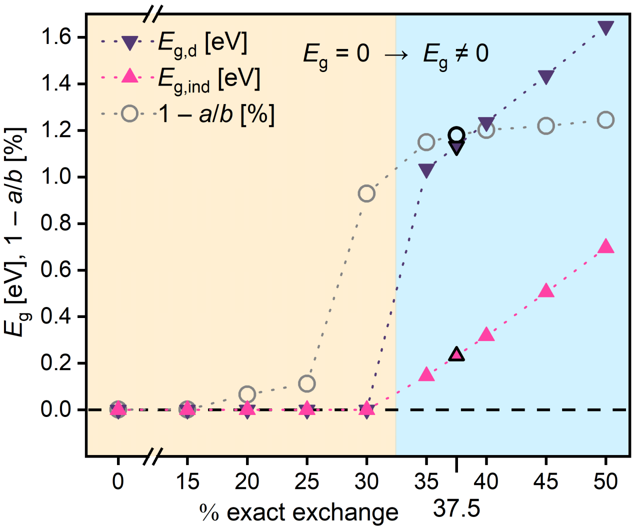

Figure 2. Direct ($E_{g,d}$, purple triangles) and indirect band gap ($E_{g,ind}$, pink triangles), and unit cell asymmetry (1 – a/b; grey circles) of ZnP at different levels of EE, obtained using PBExx, where xx indicates the amount of exact exchange. Metallic conductors are shown in orange, and semiconductors in blue. Results obtained using PBE38 are outlined in black.

ZnP and antiaromatic molecules. The symmetry breaking and gap-opening in **ZnP** may be rationalized by comparing it to antiaromatic ($4n$) annulenes, where n is the number of carbon atoms. In the absence of bond length alternation (BLA), $4n$ annulenes such as cyclobutadiene ($n = 1$) or planar cyclooctatetraene ($n = 2$) have a half-filled degenerate orbital pair related by a 90° rotation (i.e. sine and cosine solutions of the Hückel model; Figure 3a). This D_{4nh} configuration is unstable; in fact, it is a transition structure connecting two equivalent broken symmetry D_{2nh} minima, which have nonzero BLA.[36, 37] Introducing BLA breaks the degeneracy of the orbital pair, with one orbital (with density on shorter bonds) becoming occupied (i.e., the HOMO), and the other (with density on longer bonds) unoccupied (i.e., the LUMO; Figure 3a). As a result, the extent of BLA in $4n$ annulenes directly affects their HOMO-LUMO gap.

The band structure of D_{4h} **ZnP** shows two half-filled bands related by a 90° rotation (Figure 3b). They are responsible for its metallic conductivity. At the M reciprocal space point, at which the wavefunction is periodic with respect to the square 2×2 porphene fragment which contains the antiaromatic eight-membered circuit (whole structure in Figure 1b), these two bands are exactly degenerate. Breaking the D_{4h} symmetry by introducing BLA lowers the energy of the band concordant with the introduced BLA pattern (making more of it filled) and increases the energy of its rotational partner (making less of it filled), in a direct analogy to symmetry breaking in cyclobutadiene (Figure 3). When this Peierls distortion is sufficiently large, a metal to insulator transition occurs (Figure 3b right). Therefore, **ZnP** is an antiaromatic 2D polymer, characterized by two equivalent semiconductive D_{2h} minima connected by a gapless D_{4h} transition structure.

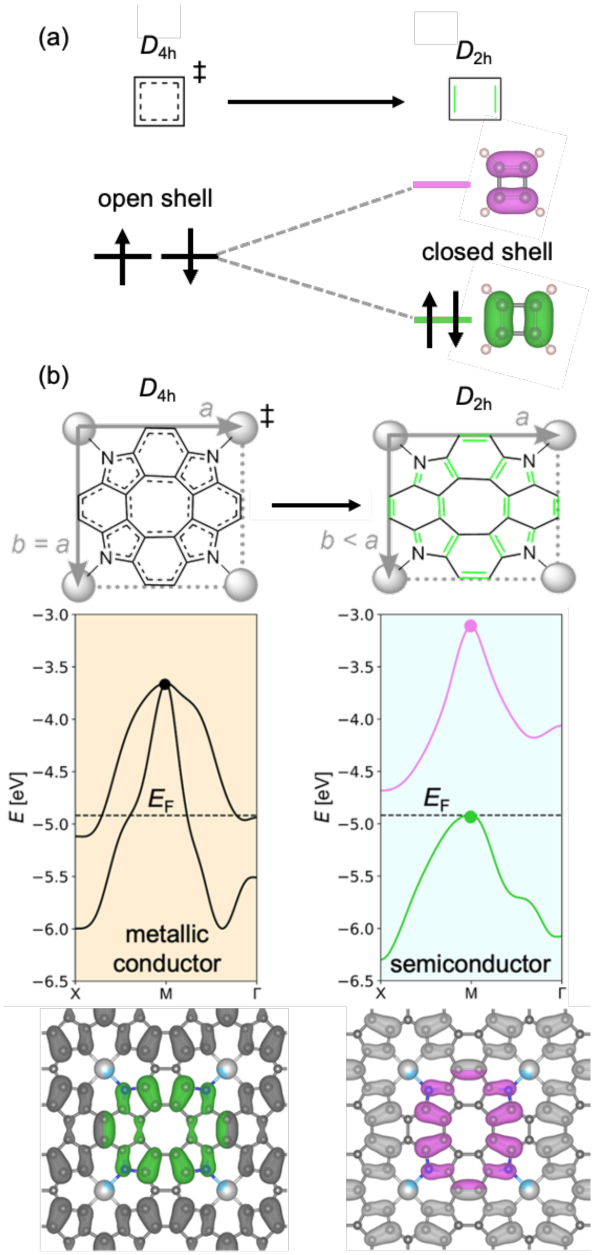

Figure 3. (a) Symmetry breaking in cyclobutadiene. (b) Peierls distortion in ZnP. Density of frontier bands in ZnP in D_{2h} geometry at the M reciprocal space point. Density associated with highest occupied and lowest unoccupied orbitals or bands is shown in green and pink, respectively.

B. First transition row metalloporphenes. To understand the effect of inserting different metals into porphene, we have investigated 36 first row metalloporphenes in their D_{2h} and D_{4h} minima. These metalloporphenes can be described with the general formula $^{2S+1}M(q)XP$, where the metal M, which is in oxidation state q, ranges from Sc to Zn. X denotes the axial ligand (oxide or chloride, if present) and 2S+1 the unit cell multiplicity. In addition to band structures, we report the band gap E_g, effective masses m_e (in semiconductors) and conductivity (in gapless systems), the energy difference between the lowest-energy D_{2h} and D_{4h} geometries (when they are distinct), and the work function. Finally, the variation in C–C bond lengths is described with a modified HOMA.[38, 39] Further details are given in the experimental section.

In virtually all cases, we found that the bands close to the Fermi level have a dominant π character (Figures 5 and 6), indicating that the analogy between metalloporphenes and annulenes may be generally valid. This motivated us to classify the metalloporphenes according to the number of π electrons in their unit cell (Table 1). Chart 1 displays a "periodic table" of first transition row metalloporphenes, showcasing a variety of open- and closed-shell metallic conductors and semiconductors.

Most metalloporphenes, including **Zn(II)P**, belong to group **0**, in which the number of π-electrons remains unperturbed by the presence of the metal. Therefore, all group **0** metalloporphenes have 26 π electrons per unit cell and display antiaromatic features. They can be divided further according to the extent of electron delocalization, or ascending U/t ratio: $\mathbf{0^{tt}}$ (no Peierls distortion, gapless), $\mathbf{0^{t}}$ (distorted, gapless), $\mathbf{0^{U}}$ (antiaromatic semiconductors), and $\mathbf{0^{UU}}$ (Baird aromatic semiconductors), as shown in Figure 4.

In group **–1** (25 π electrons per unit cell), an electron is transferred from the π system into a low-energy d orbital, while in group **1** (27 π e$^-$) an electron is donated from a high-energy d orbital into the π system. Members of both **–1** and **1** are half-metals, which may be compared to open-shell radical cations (group **–1**) or anions (**1**) of annulenes.

The only first-transition row member of group **2** is singlet titanium porphene, in which titanium donates both of its d electrons to the π system, resulting in 28 π-electrons per unit cell and a metalloporphene which may be written as $\mathbf{^{1}Ti(IV)^{4+}P^{4-}}$. Adding two electrons to conjugated hydrocarbons usually reverses their aromaticity,[40, 41] so it is not surprising that $\mathbf{^{1}Ti(IV)^{4+}P^{4-}}$ shows behavior consistent with an aromatic compound.

Table 1. Classification of Metalloporphenes.

grp	n_π[a]	S/M[b]	sym[c]	metalloporphene
–1	25	M	D_{4h}	$\mathbf{^{2}V(III)^{+}Cl_2P^{-}}$, $\mathbf{^{5}Fe(III)^{+}Cl_2P^{-}}$, $\mathbf{^{4}Co(I)^{+}P^{-}}$, $^{5}Fe(III)^{+}OP^{-}$
$\mathbf{0^{tt}}$	26	M	D_{4h}	$\mathbf{^{1}Ti(IV)Cl_2P}$, $^{4}Cr(III)ClP$
$\mathbf{0^{t}}$	26	M	D_{2h}	$^{1}Co(III)ClP$, $\mathbf{^{1}Ni(II)P}$, $^{2}Mn(II)P$, $^{2}FeCl(III)P$, $\mathbf{^{6}FeCl(III)P}$, $^{2}Co(II)P$, $^{5}CoCl(III)P$, $\mathbf{^{2}Cu(II)P}$, $^{5}Cr(II)P$
$\mathbf{0^{U}}$	26	S	D_{2h}	$\mathbf{^{1}Mg(II)P}$, $\mathbf{^{1}ScCl(III)P}$, $^{1}Cr(II)P$, $^{1}Fe(II)P$, $\mathbf{^{5}Fe(II)P}$, $\mathbf{^{1}Zn(II)P}$, $^{1}Fe(IV)Cl_2P$
$\mathbf{0^{UU}}$	26	S	D_{2h}	$\mathbf{^{2}Cr(III)ClP}$, $\mathbf{^{3}Fe(IV)OP}$
			D_{4h}	$^{3}Co(III)ClP$, $\mathbf{^{3}Cr(II)P}$, $^{2}V(II)P$
1	27	M	D_{2h}	$\mathbf{^{2}Sc(III)^{3+}P^{3-}}$, $\mathbf{^{4}V(III)^{3+}P^{3-}}$
			D_{4h}	$\mathbf{^{3}Ti(III)^{3+}P^{3-}}$, $\mathbf{^{4}Mn(III)^{3+}P^{3-}}$, $^{6}Mn(III)^{3+}P^{3-}$, $^{3}Fe(III)^{3+}P^{3-}$
2	28	S	D_{4h}	$^{1}Ti(IV)^{4+}P^{4-}$

Bold: lowest-energy spin state for this combination of metal and ligand. Orange: metallic conductors; blue: semiconductors.

[a] Number of π-electrons in the unit cell; [b] Presence (S) or absence (M) of a band gap; [c] Point group of the lowest minimum.

To emphasize electron transfer, formulas of metalloporphenes in groups **–1**, **1**, and **2** in are written as in the example above. In Figure 4, minimal band structures for each metalloporphene group are shown, alongside analogous frontier MO diagrams. Throughout the text, metallic conductors are shown in orange and semiconductors in blue. The next section provides an overview of metalloporphene groups with a few examples; data for all systems can be found in the SI.

Chart 1. Most stable electronic states of first row metalloporphenes.

axial ligand	metalloporphene											
	*d*¹	*d*²	*d*³	*d*⁴	*d*⁵		*d*⁶		*d*⁷	*d*⁸	*d*⁹	*d*¹⁰
none	^{2}ScP	^{3}TiP	^{4}VP	^{3}CrP	^{4}MnP		^{5}FeP		^{4}CoP	^{1}NiP	^{2}CuP	^{1}ZnP
		^{1}TiP* [0.29]*	^{2}VP [0.21]	^{5}CrP [0.36]	^{6}MnP [0.14]		^{3}FeP [0.04]		^{2}CoP [0.21]			
Cl, O	^{1}ScClP	^{1}TiCl$_2$P	^{2}VCl$_2$P	^{2}CrClP		^{6}FeClP	^{5}FeCl$_2$P	^{3}FeOP	^{3}CoClP			
						^{2}FeClP [0.35]		^{5}FeOP [0.01]	^{1}CoClP [0.48]			

Gapless metalloporphenes are shown in blue, and semiconductors in orange; closed-shell singlets are shown with a grey background. * Spin states within 0.5 eV/unit cell relative to the most stable state, with relative energy in brackets.

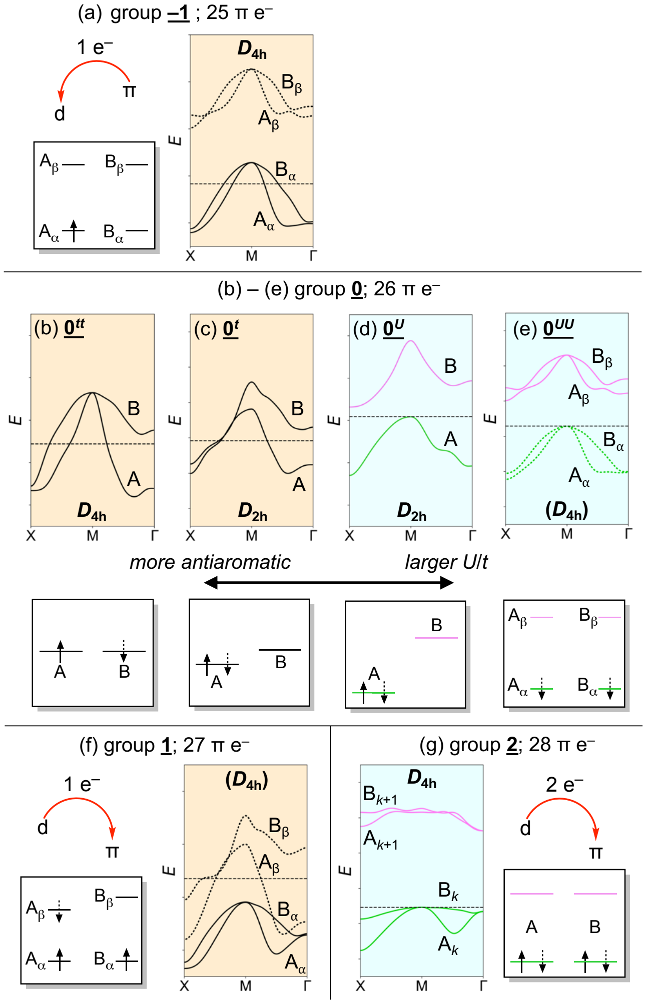

Figure 4. Minimal band structures and analogous MO diagrams for metalloporphenes in groups $\underline{\mathbf{-1}}$ (a), $\underline{\mathbf{0}}^{tt}$ (b), $\underline{\mathbf{0}}^{t}$ (c), $\underline{\mathbf{0}}^{U}$ (d), $\underline{\mathbf{0}}^{UU}$ (e), $\underline{\mathbf{1}}$ (f), and $\underline{\mathbf{2}}$ (g), showing only bands close to the Fermi level along X-M-Γ, and frontier molecular orbitals. In spin-polarized systems, dashed (full) lines and arrows correspond to α (β) spin.

Group $\underline{\mathbf{0}}$. All metalloporphenes in group $\underline{\mathbf{0}}$ have 26 π-electrons but differ significantly in electronic structure and properties. Members of $\underline{\mathbf{0}}^{tt}$ always feature axial ligands and have (mostly) empty *d*-shells (e.g. **^{1}Ti(IV)Cl$_2$P**, Figure 5a). They optimize to D_{4h} minima, which results in two half-filled bands degenerate at the M point (Figure 4b and 5a) and leads to metallic conductivity. These features are consistent with a small U/t ratio ($U \approx 0$), which prevents the Peierls distortion and consequently the gap-opening (bond length variation is still present, cf. HOMA values in Table 2). Members of $\underline{\mathbf{0}}^{tt}$ may be compared to D_{4h} cyclobutadiene (Figure 4b bottom), in which the rotationally related orbitals A and B share two opposite-spin electrons, leading to an open-shell singlet with very strong antiaromaticity.

Members of $\underline{\mathbf{0}}^{t}$ are formed with metals which have at least a half-filled *d*-shell (Mn–Cu). They undergo a Peierls distortion to D_{2h}, which breaks the band degeneracy at the M point (Figure 4c), but which is insufficiently large to open a band gap. This may be attributed to a slightly larger U/t ratio compared to $\underline{\mathbf{0}}^{tt}$, resulting a marginally more localized electronic structure. An analogous annulene would be cyclobutadiene with very slight BLA (Figure 4c bottom), in which both open-shell character and antiaromaticity are slightly reduced relative to $\underline{\mathbf{0}}^{tt}$. Compared to other metalloporphenes, members of $\underline{\mathbf{0}}^{tt}$ and $\underline{\mathbf{0}}^{t}$ tend to have relatively high work functions and conductivities (Table 2).

^{1}Zn(II)P (Figure 5c) belongs to the $\underline{\mathbf{0}}^{U}$ group, in which electron repulsion is sufficiently large to both induce a distortion and to open a band gap. This corresponds to a closed-shell electronic structure in cyclobutadiene at its equilibrium geometry (Figure 4d). The relatively high U/t ratio in $\underline{\mathbf{0}}^{U}$ is reflected in large effective masses (corresponding to poorer electron mobility; Table 3), compared to similar porphyrin-based systems.[42]

Table 2. Properties of selected gapless metalloporphenes.

grp	cmpd	Δ*E*^{a}	*W*^{b}	*σ*^{c}	HOMA
$\underline{\mathbf{-1}}$	^{2}V(III)$^+$Cl$_2$P$^-$	0	6.17	0.33	0.65
	^{5}Fe(III)$^+$Cl$_2$P$^-$		6.58	0.84	0.41
	^{4}Co(I)$^+$P$^-$		5.53	0.46	0.64
$\underline{\mathbf{0}}^{tt}$	^{1}TiCl$_2$P	0	6.20	0.94	0.01
$\underline{\mathbf{0}}^{t}$	^{6}FeClP	0.03	5.57	0.49	0.41
	^{1}NiP	0.01	5.08	0.91	0.40
	^{2}CuP	0.05	4.90	0.47	0.39
$\underline{\mathbf{1}}$	^{2}Sc(III)$^{3+}$P^{3-}	0.01	4.65	0.31	0.70
	^{3}Ti(III)$^{3+}$P^{3-}	0.40	4.84	0.26	0.90
	^{4}V(III)$^{3+}$P^{3-}	0.68	4.77	0.23	0.92
	^{4}Mn(III)$^{3+}$P^{3-}	<0.01	4.93	0.29	0.09

[a] Energy difference between the D_{4h} and D_{2h} minima (eV). [b] work function (eV); [c] conductivity (MS/m)

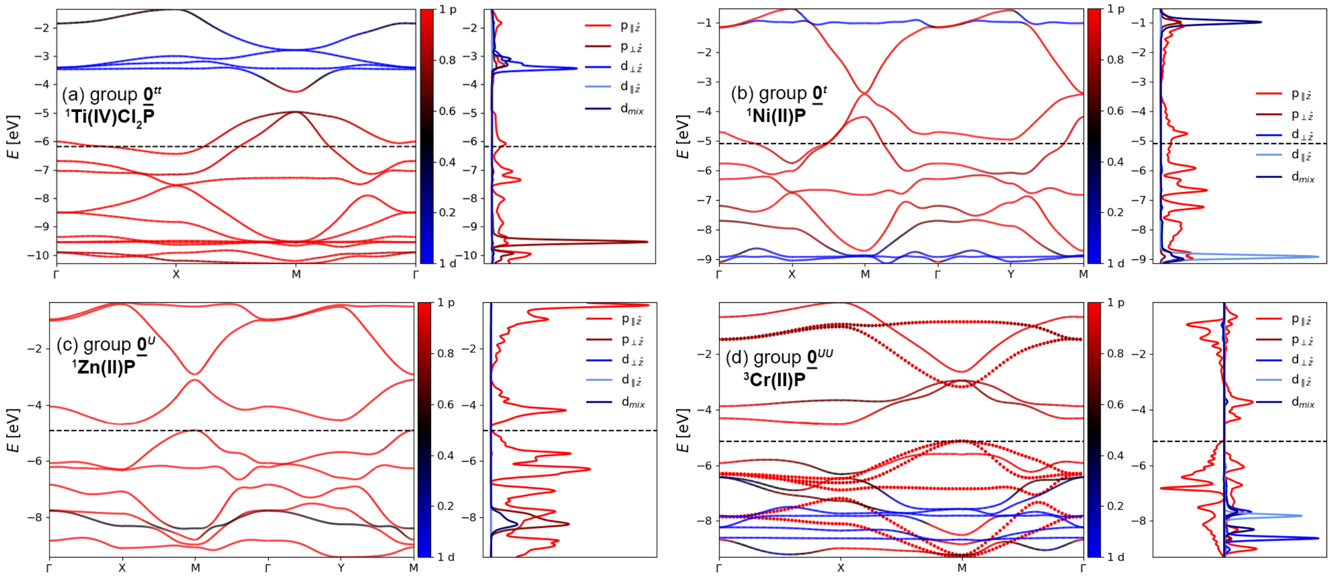

Figure 5. Band diagrams and density of states plots for (a) ^{1}**Ti(IV)Cl₂P** ($\underline{\mathbf{0}}^{tt}$, D_{4h} geometry), (b) ^{1}**NiP** ($\underline{\mathbf{0}}^{t}$, D_{2h}), (c) ^{1}**Zn(II)P** ($\underline{\mathbf{0}}^{U}$, D_{2h}), and (d) ^{3}**Cr(II)P** ($\underline{\mathbf{0}}^{UU}$, D_{2h}). Red and blue colors denote *p* and *d* band character, respectively; black dashed line shows the Fermi level (top of valence band in semiconductors). In spin-polarized systems, different spins are shown with dotted and full lines in the band diagram and as positive and negative values in the density of states plots.

In the lowest triplet state of cyclobutadiene, both rotationally related orbitals A and B are singly occupied with same-spin electrons, resulting in a Baird aromatic D_{4h} geometry (Figure 4e bottom). If U is sufficiently large, the triplet can even become the ground state, as found in some indenofluorenees.[43,44] This is analogous to the electronic structure of $\underline{\mathbf{0}}^{UU}$ metalloporphenes (Figure 4e), which must be spin-polarized. As the frontier bands in $\underline{\mathbf{0}}^{U}$ are spatially almost identical, these metalloporphenes have similar electron and hole mobilities. Due to their Baird aromatic character, they tend to have significantly larger band gaps and smaller BLA than $\underline{\mathbf{0}}^{U}$ metalloporphenes (Table 3).

Table 3. Properties of selected gapful metalloporphenes.

grp	cmpd.	$E_{g,i}$[a] $E_{g,d}$	ΔE[b]	W[c]	m_{VB}[d] m_{CB}	HOMA
$\underline{\mathbf{0}}^{U}$	^{1}**ScClP**	0.31 1.21	0.06	5.77	0.19 0.37	0.02
	^{5}**FeP**	0.48 3.07	0.43	4.89	0.17 0.23	0.09
	^{1}**ZnP**	0.22 1.13	0.10	4.91	0.18 0.41	0.04
$\underline{\mathbf{0}}^{UU}$	^{2}**CrClP**	0.77 2.22	2.78	5.88	0.24 0.16	0.64
	^{3}**CrP**	0.61 2.12	0	5.13	0.22 0.15	0.66
	^{3}**CoClP**	0.82 2.58	0	5.68	0.25 0.20	0.59
$\underline{\mathbf{2}}$	^{1}**Ti(VI)$^{4+}$P^{4-}**	2.17 2.28	0	5.54	1.20 0.42	0.74

[a] Indirect ($E_{g,i}$) and direct ($E_{g,d}$) band gap.
[b] Energy difference between the D_{4h} and D_{2h} minima (eV).
[c] work function (eV); [d] valence (m_{VB}) and conduction (m_{CB}) eff. mass

Groups $\underline{\mathbf{-1}}$ and $\underline{\mathbf{1}}$. When the transition metal inserted into porphene has a vacant low-lying d orbital, an electron can be transferred from the π- to the d-system, resulting in a group $\underline{\mathbf{-1}}$ metalloporphene (Figure 4a). One such example is cobalt porphene in its quartet state (Figure 6a). If we assume cobalt is divalent, it will have a singly occupied low-energy d_{xy} orbital which can accept a π-electron from porphene, thus making ^{4}Co(I)$^+$P$^-$.

Conversely, when the transition metal has an occupied high-energy *d*-orbital, $d \rightarrow \pi$ single-electron transfer can occur, forming a group $\underline{\mathbf{1}}$ metalloporphene. An obvious example is

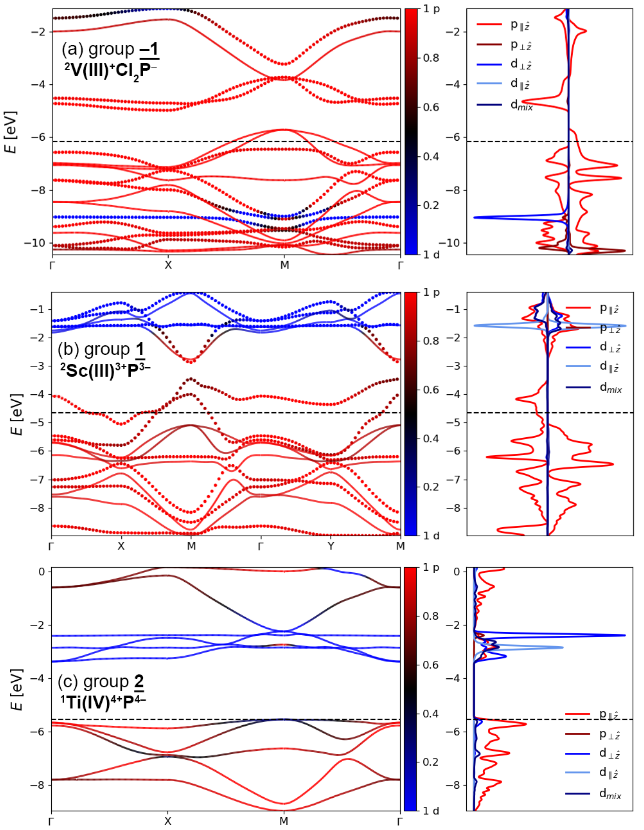

Figure 6. Band diagrams and density of states plots for (a) ^{2}V(III)$^+$Cl$_2$P$^-$ (group $\underline{\mathbf{-1}}$, D_{2h} geometry), (b) ^{2}Sc(III)$^{3+}$P^{3-} ($\underline{\mathbf{1}}$, D_{2h}), (c) ^{1}Ti(IV) $^{4+}$Cl^{4-} ($\underline{\mathbf{2}}$, D_{4h}). Red and blue colors denote p and d band character, respectively; black dashed line shows the Fermi level (top of valence band in semiconductors). In spin-polarized systems, different spins are shown with dotted and full lines in the band diagram and as positive and negative values in the density of states plots.

scandium porphene: in the absence of axial ligands, scandium will oxidize to Sc(III) by giving its electron to the π-system to form $\mathbf{^{2}Sc(III)^{3+}P^{-}}$ (Figure 6b).

These metalloporphenes may be compared to radical cations and anions of annulenes, which tend to have low BLA.[45,46] This leads to a small SOMO-SUMO gap, consistent with half-metallic behavior in groups $\underline{\mathbf{1}}$ and $\underline{\mathbf{-1}}$.

Group 2. Adding two electrons to the porphene π-system (relative to group $\underline{\mathbf{0}}$) completely fills up both rotationally related bands (Figure 4g), which leads to a D_{4h} geometry and a relatively large band gap (>2 eV, Table 3) in $\mathbf{^{1}Ti(IV)^{4+}P^{4-}}$ (Figure 6c). Its electronic structure is similar to that of benzene (Figure 4f), indicating that a general form of Huckel's rule (adding or removing two electrons reverses aromaticity) is applicable to the electronic structure of metalloporphenes. Group $\underline{\mathbf{2}}$ metalloporphenes seem to be relatively rare, probably because they require metals with very high–energy d-electrons (i.e. strong reducing agents).

Outlook. At this point, it may be useful to identify several potential areas of application for metalloporphenes:

(i) *Molecular wires.* Due to their high conductivities, group $\underline{\mathbf{0}^{tt}}$ and $\underline{\mathbf{0}^{t}}$ metalloporphenes may be useful as molecular wires. Possible diamagnetic candidates are $\mathbf{^{1}Ti(IV)Cl_2P}$ and $\mathbf{^{1}Ni(II)P}$, both of which belong to $\underline{\mathbf{0}^{t}}$. Preparing these metalloporphenes would also provide a simple test of the predictions made here.

(ii) *Tunable semiconductors.* Semiconductive metalloporphenes ($\underline{\mathbf{0}^{U}}$, $\underline{\mathbf{0}^{UU}}$, and $\underline{\mathbf{2}}$) have a large variety of band gaps (1–3 eV), making them similar to quantum dots,[47] except that the electronic properties are controlled by choice of metal instead of by size. Accurate band gap measurements (e.g. for $\mathbf{^{1}Zn(II)P}$) will also enable the validation and refinement of these computational predictions.

(iii) *Mechanical properties.* In $\underline{\mathbf{0}^{t}}$ and $\underline{\mathbf{0}^{U}}$ metalloporphenes, there exist two equivalent D_{2h} orientations of each unit cell. As the barrier for their interconversion is low (~0.1 eV/unit cell, cf. Table 2, 3, and SI), the macroscopic properties of these metalloporphenes may be governed by statistics at the macroscopic scale, and controlled by mechanical stretching.

(iv) *Patterning.* As noted previously,[14] metalloporphenes might be used to build nanoscale circuits by inserting different metals in a specific pattern. Our results suggest that $\underline{\mathbf{0}^{UU}}$ or $\underline{\mathbf{0}^{U}}$ metalloporphenes could be used as a non-conductive blank canvas, which one could pattern by inserting metals forming $\underline{\mathbf{0}^{tt}}$ and $\underline{\mathbf{0}^{t}}$ metalloporphenes.

(v) *Magnetism.* The potential for use of metalloporphenes in spintronics is currently speculative, as their magnetic ground state and exchange coupling is still unknown. Unless the exchange interaction through the π-system is very strong, the relatively large separation (~8.5 Å) between metallic centers will prevent fast decoherence,[48] which is essential for building multi-qubit devices. Fine control over the strength of the exchange coupling could be achieved by metal choice: for example, the metallic conductor $\mathbf{^{2}Cu(II)P}$ will likely have a larger coupling than the semiconducting $\mathbf{^{2}Cr(III)ClP}$. Finally, the half-metallic behavior (i.e. conduction through only a single spin channel) of groups $\underline{\mathbf{-1}}$ (e.g. $\mathbf{^{2}V(III)^{+}Cl_2P^{-}}$) and $\underline{\mathbf{1}}$ suggests applications in spin filtering.[49, 50]

Limitations. To paraphrase Imre Lakatos, the quality of a theory is determined by the accuracy of its predictions.[51] While hybrid DFT has undoubtedly been very successful in predicting properties of many materials, the procedure for choosing the ideal amount of exact exchange (or the Hubbard U) is not always clear, especially when geometry optimizations and large unit cells are involved, preventing the use of higher-level methods such as MP2 and *GW*. In case of metalloporphenes, using less than 35% EE yields a qualitatively wrong electronic structure (Figure 2), while using a significantly larger amount overestimates localization, predicting too high spin multiplicities. For instance, PBE50 wrongly predicts the ground state of iron(II) porphyrin to be a quintet, while PBE0 and PBE38 correctly predict a triplet.[52] Therefore, our choice of the "best" amount of EE is bound on both sides, and inaccuracies resulting from our choice are likely limited to subgroups of $\underline{\mathbf{0}}$ (e.g. **ZnP** is predicted to be in $\underline{\mathbf{0}^{t}}$ if 20–30% EE is used, and in group $\underline{\mathbf{0}^{tt}}$ with <20% EE, cf. Figure 1). Neglect of spin-orbit coupling may be a larger issue, but its inclusion is very costly due to the loss of time-reversal symmetry, making it impractical to perform such calculations on a large scale.

CONCLUSIONS

This paper provides a theoretical description of **ZnP** that agrees with experiment and accounts for its semiconductive nature. **ZnP** has an electronic structure analogous to antiaromatic molecules, making it susceptible to Peierls distortion. This distortion is sufficiently large to produce two equivalent semiconductive D_{2h} minima connected through a low-energy D_{4h} gapless transition structure, which can be captured with DFT only if a hybrid functional with a sufficient amount of exact exchange is used.

Exploring many first transition row metalloporphenes, we find a large variety of diamagnetic and paramagnetic semiconductors and metallic conductors, unravelling an unexplored landscape of tunable, fully conjugated 2D materials, which may show interesting electronic, mechanical, and magnetic properties. It is our hope that the classification presented here will serve as both a motivation and a guiding beacon for further investigation of these systems.

More generally, we have accounted for a large variety of metalloporphene band structures, and properties related to them, by applying the concepts of antiaromaticity and (Baird) aromaticity. Antiaromatic motifs in materials are desirable as they are often associated with low redox potentials,[53] open-shell character,[54] and high carrier mobility,[55] and this work is a step towards a deeper understanding of their electronic structure.

METHODS

DFT calculation details. All calculations were done with the VASP code.[56-58] Geometry optimizations were done using the PBE38 functional with D3BJ dispersion corrections, with a planewave kinetic energy cutoff of 420 eV, and a 6×6×1 gamma-centered grid of reciprocal space points. The polymer was positioned in the *xy* plane, and 10 Å of vacuum were added in *z* (13 Å when axial ligands were present). Total energies were converged to 0.1 meV. Finally, a single-point calculation was done at an 8×8×1 *k* grid to evaluate the electronic structure and total energy more accurately; the output of this calculation was used in subsequent analysis.

The vacuum level was determined using Vaspkit.[59] Band diagrams, effective masses, and electron mobilities were obtained by interpolating band energies obtained at the 8×8×1 *k* grid using BoltzTrap2;[60] to obtain an estimate of conductivity, the constant relaxation time approximation ($\tau = 10^{-14}$ s) was employed.

HOMA (Harmonic Oscillator Model of Aromaticity) index was calculated according to:

$$\text{HOMA} = 1 - \frac{\alpha}{n}\sum_{i=1}^{n}(R_i - \bar{R})^2$$

where α = 1682.792, R_i is the length of the *i*th C-C bond, and $\bar{R}$ is the average C-C bond length in ^{1}**TiP**. α is chosen so that the HOMA value of the D_{2h} geometry of ^{1}**MgP**, which has the highest amount of bond length variation, is equal to 0.

ASSOCIATED CONTENT

Supporting Information

The Supporting Information is available free of charge on the ACS Publications website.

- Computed band diagrams, density of states plots, and related properties of all metalloporphenes (PDF).

All optimized geometries (POSCAR) and parsable output files (vasprun.xml) are available as a Zenodo open access dataset (doi: 10.5281/zenodo.7580003).

AUTHOR INFORMATION

Corresponding Author

* igor.roncevic@chem.ox.ac.uk

ACKNOWLEDGMENT

This work was supported by the US National Science Foundation (grant CHE 1900226), the Institute of Organic Chemistry and Biochemistry of the Czech Academy of Sciences (RVO: 61388963) and the Czech Science Foundation (grant 20-03691X). IR acknowledges support by the UKRI Horizon Europe Guarantee MSCA Postdoctoral Fellowship ELDELPATH (EP/X030075/1)

Computational resources were provided by the Ministry of Education, Youth and Sports of the Czech Republic through e-INFRA CZ (ID:90140). This work used the Cirrus UK National Tier-2 HPC Service at EPCC (http://www.cirrus.ac.uk) funded by the University of Edinburgh and EPSRC (EP/P020267/1), and the Computational Centre of the Department of Chemistry, University of Zagreb, Faculty of Science, funded by the European Regional Development Fund (infrastructural project CIuK, grant number KK.01.1.1.02.0016).

REFERENCES

(1) Wang, W.; Zhao, W.; Xu, H.; Liu, S.; Huang, W.; Zhao, Q. Fabrication of ultra-thin 2d covalent organic framework nanosheets and their application in functional electronic devices. *Coordination Chemistry Reviews* **2021**, *429*, 213616. DOI: https://doi.org/10.1016/j.ccr.2020.213616

(2) Dong, R.; Zhang, T.; Feng, X. Interface-assisted synthesis of 2d materials: Trend and challenges. *Chemical Reviews* **2018**, *118*, 6189-6235. DOI: 10.1021/acs.chemrev.8b00056

(3) Colson, J. W.; Dichtel, W. R. Rationally synthesized two-dimensional polymers. *Nature Chemistry* **2013**, *5*, 453-465. DOI: 10.1038/nchem.1628

(4) Payamyar, P.; King, B. T.; Öttinger, H. C.; Schlüter, A. D. Two-dimensional polymers: Concepts and perspectives. *Chemical Communications* **2016**, *52*, 18-34. DOI: 10.1039/c5cc07381b

(5) Cai, Z.; Liu, B.; Zou, X.; Cheng, H.-M. Chemical vapor deposition growth and applications of two-dimensional materials and their heterostructures. *Chemical Reviews* **2018**, *118*, 6091-6133. DOI: 10.1021/acs.chemrev.7b00536

(6) Zeng, M.; Xiao, Y.; Liu, J.; Yang, K.; Fu, L. Exploring two-dimensional materials toward the next-generation circuits: From monomer design to assembly control. *Chemical Reviews* **2018**, *118*, 6236-6296. DOI: 10.1021/acs.chemrev.7b00633

(7) Jin, H.; Guo, C.; Liu, X.; Liu, J.; Vasileff, A.; Jiao, Y.; Zheng, Y.; Qiao, S.-Z. Emerging two-dimensional nanomaterials for electrocatalysis. *Chemical Reviews* **2018**, *118*, 6337-6408. DOI: 10.1021/acs.chemrev.7b00689

(8) Ares, P.; Novoselov, K. S. Recent advances in graphene and other 2d materials. *Nano Materials Science* **2022**, *4*, 3-9. DOI: https://doi.org/10.1016/j.nanoms.2021.05.002

(9) Novoselov, K. S.; Fal′ko, V. I.; Colombo, L.; Gellert, P. R.; Schwab, M. G.; Kim, K. A roadmap for graphene. *Nature* **2012**, *490*, 192-200. DOI: 10.1038/nature11458

(10) Allen, M. J.; Tung, V. C.; Kaner, R. B. Honeycomb carbon: A review of graphene. *Chemical Reviews* **2010**, *110*, 132-145. DOI: 10.1021/cr900070d

(11) Pumera, M.; Sofer, Z. Towards stoichiometric analogues of graphene: Graphane, fluorographene, graphol, graphene acid and others. *Chemical Society Reviews* **2017**, *46*, 4450-4463. DOI: 10.1039/C7CS00215G

(12) Matochová, D.; Medved', M.; Bakandritsos, A.; Steklý, T.; Zbořil, R.; Otyepka, M. 2d chemistry: Chemical control of graphene derivatization. *The Journal of Physical Chemistry Letters* **2018**, *9*, 3580-3585. DOI: 10.1021/acs.jpclett.8b01596

(13) Magnera, T. F.; Dron, P. I.; Bozzone, J. P.; Jovanovic, M.; Rončević, I.; Tortorici, E.; Bu, W.; Miller, E. M.; Rogers, C. T.; Michl, J. Porphene and porphite as porphyrin analogs of graphene and graphite. *Nature Communications* **2023**, *14*, 6308. DOI: 10.1038/s41467-023-41461-w

(14) Ono, Y.; Hamano, T. Peierls distortion in two-dimensional tight-binding model. *Journal of the Physical Society of Japan* **2000**, *69*, 1769-1776. DOI: 10.1143/JPSJ.69.1769

(15) Kertesz, M.; Choi, C. H.; Yang, S. Conjugated polymers and aromaticity. *Chemical Reviews* **2005**, *105*, 3448-3481. DOI: 10.1021/cr990357p

(16) Popov, I. A.; Bozhenko, K. V.; Boldyrev, A. I. Is graphene aromatic? *Nano Research* **2012**, *5*, 117-123. DOI: 10.1007/s12274-011-0192-z

(17) Zdetsis, A. D.; Economou, E. N. A pedestrian approach to the aromaticity of graphene and nanographene: Significance of huckel's (4n+2)π electron rule. *The Journal of Physical Chemistry C* **2015**, *119*, 16991-17003. DOI: 10.1021/acs.jpcc.5b04311

(18) Nakamura, Y.; Aratani, N.; Shinokubo, H.; Takagi, A.; Kawai, T.; Matsumoto, T.; Yoon, Z. S.; Kim, D. Y.; Ahn, T. K.; Kim, D.; et al. A directly fused tetrameric porphyrin sheet and its anomalous electronic properties that arise from the planar cyclooctatetraene core. *Journal of the American Chemical Society* **2006**, *128*, 4119-4127. DOI: 10.1021/ja057812l

(19) Yamaguchi, Y. Theoretical study of two-dimensionally fused zinc porphyrins: Dft calculations. *International Journal of Quantum Chemistry* **2009**, *109*, 1584-1597. DOI: https://doi.org/10.1002/qua.21998

(20) Yamaguchi, Y. Transport properties of two-dimensionally fused zinc porphyrins from linear-response approach. *International Journal of Quantum Chemistry* **2011**, *111*, 3230-3238. DOI: https://doi.org/10.1002/qua.22717

(21) Yamaguchi, Y. Theoretical prediction of electronic structures of fully pi-conjugated zinc oligoporphyrins with curved surface structures. *J Chem Phys* **2004**, *120*, 7963-7970. DOI: 10.1063/1.1690759

(22) Posligua, V.; Aziz, A.; Haver, R.; Peeks, M. D.; Anderson, H. L.; Grau-Crespo, R. Band structures of periodic porphyrin nanostructures. *The Journal of Physical Chemistry C* **2018**, *122*, 23790-23798. DOI: 10.1021/acs.jpcc.8b08131

(23) Tan, J.; Li, W.; He, X.; Zhao, M. Stable ferromagnetism and half-metallicity in two-dimensional polyporphyrin frameworks. *RSC Advances* **2013**, *3*, 7016-7022. DOI: 10.1039/C3RA40502H

(24) Liu, J.-H.; Yang, L.-M.; Ganz, E. Electrocatalytic reduction of co2 by two-dimensional transition metal porphyrin sheets. *Journal of*

Materials Chemistry A **2019**, *7*, 11944-11952. DOI: 10.1039/C9TA01188A

(25) Glöcklhofer, F. Concealed antiaromaticity. *ChemRxiv* **2023**. DOI: 10.26434/chemrxiv-2023-hnl0w-v2

(26) Ono, S. Two-dimensional square lattice polonium stabilized by the spin–orbit coupling. *Scientific Reports* **2020**, *10*, 11810. DOI: 10.1038/s41598-020-68877-4

(27) Nevalaita, J.; Koskinen, P. Atlas for the properties of elemental two-dimensional metals. *Physical Review B* **2018**, *97*, 035411. DOI: 10.1103/PhysRevB.97.035411

(28) Arovas, D. P.; Berg, E.; Kivelson, S. A.; Raghu, S. The hubbard model. *Annual Review of Condensed Matter Physics* **2022**, *13*, 239-274. DOI: 10.1146/annurev-conmatphys-031620-102024

(29) Zaffran, J.; Caspary Toroker, M. Benchmarking density functional theory based methods to model niooh material properties: Hubbard and van der waals corrections vs hybrid functionals. *Journal of Chemical Theory and Computation* **2016**, *12*, 3807-3812. DOI: 10.1021/acs.jctc.6b00657

(30) Cohen, A. J.; Mori-Sánchez, P.; Yang, W. Insights into current limitations of density functional theory. *Science* **2008**, *321*, 792-794. DOI: 10.1126/science.1158722

(31) Perdew, J. P.; Burke, K.; Ernzerhof, M. Generalized gradient approximation made simple. *Physical Review Letters* **1996**, *77*, 3865-3868. DOI: 10.1103/PhysRevLett.77.3865

(32) Baryshnikov, G. V.; Valiev, R. R.; Kuklin, A. V.; Sundholm, D.; Ågren, H. Cyclo[18]carbon: Insight into electronic structure, aromaticity, and surface coupling. *The Journal of Physical Chemistry Letters* **2019**, *10*, 6701-6705. DOI: 10.1021/acs.jpclett.9b02815

(33) Deng, J.-R.; Bradley, D.; Jirásek, M.; Anderson, H. L.; Peeks, M. D. Correspondence on “how aromatic are molecular nanorings? The case of a six-porphyrin nanoring”**. *Angewandte Chemie International Edition* **2022**, *61*, e202201231. DOI: https://doi.org/10.1002/anie.202201231

(34) Grimme, S.; Hansen, A.; Brandenburg, J. G.; Bannwarth, C. Dispersion-corrected mean-field electronic structure methods. *Chemical Reviews* **2016**, *116*, 5105-5154. DOI: 10.1021/acs.chemrev.5b00533

(35) Santra, G.; Martin, J. M. L. What types of chemical problems benefit from density-corrected dft? A probe using an extensive and chemically diverse test suite. *Journal of Chemical Theory and Computation* **2021**, *17*, 1368-1379. DOI: 10.1021/acs.jctc.0c01055

(36) Monino, E.; Boggio-Pasqua, M.; Scemama, A.; Jacquemin, D.; Loos, P.-F. Reference energies for cyclobutadiene: Automerization and excited states. *The Journal of Physical Chemistry A* **2022**, *126*, 4664-4679. DOI: 10.1021/acs.jpca.2c02480

(37) Wenthold, P. G.; Hrovat, D. A.; Borden, W. T.; Lineberger, W. C. Transition-state spectroscopy of cyclooctatetraene. *Science* **1996**, *272*, 1456-1459. DOI: 10.1126/science.272.5267.1456

(38) Krygowski, T. M.; Szatylowicz, H.; Stasyuk, O. A.; Dominikowska, J.; Palusiak, M. Aromaticity from the viewpoint of molecular geometry: Application to planar systems. *Chemical Reviews* **2014**, *114*, 6383-6422. DOI: 10.1021/cr400252h

(39) Kruszewski, J.; Krygowski, T. M. Definition of aromaticity basing on the harmonic oscillator model. *Tetrahedron Letters* **1972**, *13*, 3839-3842. DOI: https://doi.org/10.1016/S0040-4039(01)94175-9

(40) Zhou, Z.; Petrukhina, M. A. Planar, curved and twisted molecular nanographenes: Reduction-induced alkali metal coordination. *Coordination Chemistry Reviews* **2023**, *486*, 215144. DOI: https://doi.org/10.1016/j.ccr.2023.215144

(41) Zabula, A. V.; Spisak, S. N.; Filatov, A. S.; Rogachev, A. Y.; Petrukhina, M. A. Record alkali metal intercalation by highly charged corannulene. *Accounts of Chemical Research* **2018**, *51*, 1541-1549. DOI: 10.1021/acs.accounts.8b00141

(42) Zhu, H.; Chen, Q.; Rončević, I.; Christensen, K. E.; Anderson, H. L. Anthracene-porphyrin nanoribbons. *Angewandte Chemie International Edition n/a*, e202307035. DOI: 10.1002/anie.202307035

(43) Barker, J. E.; Dressler, J. J.; Cárdenas Valdivia, A.; Kishi, R.; Strand, E. T.; Zakharov, L. N.; MacMillan, S. N.; Gómez-García, C. J.; Nakano, M.; Casado, J.; Haley, M. M. Molecule isomerism modulates the diradical properties of stable singlet diradicaloids. *Journal of the American Chemical Society* **2020**, *142*, 1548-1555. DOI: 10.1021/jacs.9b11898

(44) Shantanu Mishra, M. V.-V., Leonard-Alexander Lieske, Leonard-Alexander Lieske, Igor Rončević, Florian Albrecht, Thomas Frederiksen, Diego Peña, Leo Gross. Bistability between pi-diradical open-shell and closed-shell states in indeno[1,2-a]fluorene. *arXiv* **2023**. DOI: https://doi.org/10.48550/arXiv.2303.04483

(45) Tachikawa, H. Jahn–teller effect of the benzene radical cation: A direct ab initio molecular dynamics study. *The Journal of Physical Chemistry A* **2018**, *122*, 4121-4129. DOI: 10.1021/acs.jpca.8b00292

(46) Bazante, A. P.; Davidson, E. R.; Bartlett, R. J. The benzene radical anion: A computationally demanding prototype for aromatic anions. *The Journal of Chemical Physics* **2015**, *142*, 204304. DOI: 10.1063/1.4921261

(47) García de Arquer, F. P.; Talapin, D. V.; Klimov, V. I.; Arakawa, Y.; Bayer, M.; Sargent, E. H. Semiconductor quantum dots: Technological progress and future challenges. *Science* **2021**, *373*, eaaz8541. DOI: doi:10.1126/science.aaz8541

(48) Gaita-Ariño, A.; Luis, F.; Hill, S.; Coronado, E. Molecular spins for quantum computation. *Nature Chemistry* **2019**, *11*, 301-309. DOI: 10.1038/s41557-019-0232-y

(49) Hirohata, A.; Yamada, K.; Nakatani, Y.; Prejbeanu, I.-L.; Diény, B.; Pirro, P.; Hillebrands, B. Review on spintronics: Principles and device applications. *Journal of Magnetism and Magnetic Materials* **2020**, *509*, 166711. DOI: https://doi.org/10.1016/j.jmmm.2020.166711

(50) Zatko, V.; Dubois, S. M. M.; Godel, F.; Galbiati, M.; Peiro, J.; Sander, A.; Carretero, C.; Vecchiola, A.; Collin, S.; Bouzehouane, K.; et al. Almost perfect spin filtering in graphene-based magnetic tunnel junctions. *ACS Nano* **2022**, *16*, 14007-14016. DOI: 10.1021/acsnano.2c03625

(51) Lakatos, I. *The methodology of scientific research programmes: Philosophical papers*; Cambridge University Press, 1978. DOI: DOI: 10.1017/CBO9780511621123.

(52) Zhou, C.; Gagliardi, L.; Truhlar, D. G. Multiconfiguration pair-density functional theory for iron porphyrin with cas, ras, and dmrg active spaces. *The Journal of Physical Chemistry A* **2019**, *123*, 3389-3394. DOI: 10.1021/acs.jpca.8b12479

(53) Lin, Z.; Lin, L.; Zhu, J.; Wu, W.; Yang, X.; Sun, X. An anti-aromatic covalent organic framework cathode with dual-redox centers for rechargeable aqueous zinc batteries. *ACS Applied Materials & Interfaces* **2022**, *14*, 38689-38695. DOI: 10.1021/acsami.2c08170

(54) Di Giovannantonio, M.; Eimre, K.; Yakutovich, A. V.; Chen, Q.; Mishra, S.; Urgel, J. I.; Pignedoli, C. A.; Ruffieux, P.; Müllen, K.; Narita, A.; Fasel, R. On-surface synthesis of antiaromatic and open-shell indeno[2,1-b]fluorene polymers and their lateral fusion into porous ribbons. *Journal of the American Chemical Society* **2019**, *141*, 12346-12354. DOI: 10.1021/jacs.9b05335

(55) Ukai, S.; Takamatsu, A.; Nobuoka, M.; Tsutsui, Y.; Fukui, N.; Ogi, S.; Seki, S.; Yamaguchi, S.; Shinokubo, H. A supramolecular polymer constituted of antiaromatic niii norcorroles. *Angewandte Chemie International Edition* **2022**, *61*, e202114230. DOI: https://doi.org/10.1002/anie.202114230

(56) Kresse, G.; Furthmüller, J. Efficiency of ab-initio total energy calculations for metals and semiconductors using a plane-wave basis set. *Computational Materials Science* **1996**, *6*, 15-50. DOI: https://doi.org/10.1016/0927-0256(96)00008-0

(57) Kresse, G.; Furthmüller, J. Efficient iterative schemes for ab initio total-energy calculations using a plane-wave basis set. *Physical Review B* **1996**, *54*, 11169-11186. DOI: 10.1103/PhysRevB.54.11169

(58) Kresse, G.; Hafner, J. Ab initio molecular dynamics for liquid metals. *Physical Review B* **1993**, *47*, 558-561. DOI: 10.1103/PhysRevB.47.558

(59) Wang, V.; Xu, N.; Liu, J.-C.; Tang, G.; Geng, W.-T. Vaspkit: A user-friendly interface facilitating high-throughput computing and analysis using vasp code. *Computer Physics Communications* **2021**, *267*, 108033. DOI: https://doi.org/10.1016/j.cpc.2021.108033

(60) Madsen, G. K. H.; Carrete, J.; Verstraete, M. J. Boltztrap2, a program for interpolating band structures and calculating semi-classical transport coefficients. *Computer Physics Communications* **2018**, *231*, 140-145. DOI: https://doi.org/10.1016/j.cpc.2018.05.010